Plasmid encoding *miRNA-200c* delivered by CaCO₃-based nanoparticles enhances rat alveolar bone formation

Matthew T Remy[1,2] , Qiong Ding[1] , Tadkamol Krongbaramee[1,3] , Jue Hu[1] , Andrés V Mora Mata[4] , Amanda J Haes[4] , Brad A Amendt[1,5,6] , Hongli Sun[1] , Marisa R Buchakjian[7] & Liu Hong*,[1,6]

[1]Iowa Institute for Oral Health Research, College of Dentistry, University of Iowa, Iowa City, IA 52242, USA
[2]Roy J. Carver Department of Biomedical Engineering, College of Engineering, University of Iowa, Iowa City, IA 52242, USA
[3]Division of Endodontics, Department of Restorative Dentistry & Periodontology, Faculty of Dentistry, Chiang Mai University, Chiang Mai, Thailand
[4]Department of Chemistry, College of Liberal Arts & Sciences, University of Iowa, Iowa City, IA 52242, USA
[5]Department of Anatomy & Cell Biology, Carver College of Medicine, University of Iowa, Iowa City, IA 52242, USA
[6]Center for Craniofacial Anomalies Research, Carver College of Medicine, University of Iowa, Iowa City, IA 52242, USA
[7]Department of Otolaryngology–Head & Neck Surgery, Carver College of Medicine, University of Iowa, Iowa City, IA 52242, USA
*Author for correspondence: Tel.: +1 319 384 1756; liu-hong@uiowa.edu

Aim: miRNAs have been shown to improve the restoration of craniofacial bone defects. This work aimed to enhance transfection efficiency and *miR-200c*-induced bone formation in alveolar bone defects via plasmid DNA encoding *miR-200c* delivery from CaCO₃ nanoparticles. **Materials & methods:** The CaCO₃/*miR-200c* delivery system was evaluated *in vitro* (microscopy, transfection efficiency, biocompatibility) and *miR-200c*-induced *in vivo* alveolar bone formation was assessed via micro-computed tomography and histology. **Results:** CaCO₃ nanoparticles significantly enhanced the transfection of plasmid DNA encoding *miR-200c* without inflammatory effects and sustained *miR-200c* expression. CaCO₃/*miR-200c* treatment *in vivo* significantly increased bone formation in rat alveolar bone defects. **Conclusion:** CaCO₃ nanoparticles enhance *miR-200c* delivery to accelerate alveolar bone formation, thereby demonstrating the application of CaCO₃/*miR-200c* to craniofacial bone defects.

Plain language summary: The restoration of craniofacial bone defects is surgically complex and requires the combined use of bone grafts and regenerative biomaterials. miRNAs are small biomolecules that have been shown to improve bone regeneration in large bone defects. The aim of this work was to develop a nanoparticle-based delivery system to sustain the release of miRNAs to improve the restoration of craniofacial bone defects. The results of this study demonstrated that CaCO₃ nanoparticles extend the delivery of miRNAs to enhance bone formation in a craniofacial bone defect animal model in a therapeutically safe manner that improves upon conventional nanoparticle materials for bone regeneration. The findings attest to the regenerative properties of miRNAs and further indicate the potential application of CaCO₃-based nanoparticles in restoring large bone defects.

Oral and craniofacial bone reconstruction after oral cavity cancer excision represents a significant challenge for surgeons. More than 20% of oral cancer patients present with bone invasion that requires maxillectomy or mandibulectomy and subsequent osseous reconstruction [1–3]. Vascularized bone grafts and osteocutaneous free flaps are the current gold-standard treatment for surgical reconstruction [4–6]. However, the surgical challenges associated with vascularized bony reconstructions are technically demanding, with craniofacial reconstructive surgeries demonstrating a nearly 40% failure and complication rate due to infections, hardware malfunction, osseous malunion and autologous bone resorption [7]. When failure occurs, patients requiring a second surgery are at fur-

Future Medicine

ther risk of complications, including increased donor site morbidity and risk of infection [8]. In addition, patients suffering from oral cancer with oral-craniofacial reconstruction often require adjuvant radiotherapy. Radiotherapy may impair bone formation and graft osseointegration and ultimately lead to graft loss [9]. Although exogenous osteogenic factors, such as US FDA-approved bone morphogenetic proteins (BMPs; RHBMP-2/7), are incorporated into grafts to promote bone regeneration at the defect site, BMPs are unstable and their short half-life requires supraphysiological dose administration, which has been linked to adverse side effects, including ectopic bone formation, bone resorption and other pro-oncogenic concerns [10–14]. Furthermore, in patients treated for oral and neck cancers, approximately two-thirds of all patients experience tumor relapse, with most cases occurring less than 1 year after primary tumor resection [15]. Thus, a safer and more effective therapeutic with strong bone regeneration and anticancer properties is needed to improve the clinical outcomes of craniofacial reconstruction for oral cancer patients.

In considering agents to combat these regeneration and restoration challenges, miRNAs (miRs) have recently emerged as tools to promote osteogenic differentiation and bone formation [16,17]. miRs are small, noncoding RNAs that play crucial roles in craniofacial bone metabolism and remodeling by epigenetically regulating biological processes, including cell cycle regulation, differentiation, migration and apoptosis [18,19]. Moreover, by targeting inhibitory regulators of osteogenic differentiation, some specific miRs have been found to upregulate the WNT/β-catenin and BMP/SMAD signaling pathways to promote bone formation [20]. In particular, *miR-200c*, a member of the miR-200 family, has been found to have anticancer and enhanced bone regeneration capabilities that inhibit bone loss, improve osteogenic differentiation of bone marrow mesenchymal stem cells (BMSCs), and promote *in vivo* bone regeneration in critical-sized calvarial defect animal models [21,22]. Previous studies have found that *miR-200c* effectively improves osteogenic differentiation and bone formation by targeting multiple components of the osteogenesis pathway, including NOGGIN (a BMP antagonist), SOX2 (a WNT signaling antagonist), AKT/β-catenin and SMAD7 [20,23]. *miR-200c* additionally possesses potent anticancer properties that inhibit the epithelial-to-mesenchymal transition in oral cancer initiation and metastases [24–27]. Furthermore, *miR-200c* has been found to suppress multiple proinflammatory cytokines and mediators, including *IL-6*, *IL-8*, *CCL-5* and *IFRγ-1*, that activate bone resorption by stimulating osteoclastogenesis [28–31]. The authors' previous work has effectively demonstrated the osteogenic and anti-inflammatory properties of using naked plasmid DNA (pDNA) encoding *miR-200c* to improve *in vivo* bone formation and regeneration in calvarial animal models; however, the capacity of *miR-200c* to regenerate bone in defect models that more appropriately mimic the conditions of oral-craniofacial reconstructive surgery, as in an alveolar bone defect model, has yet to be evaluated.

The restoration of large bone defects from tumor excisions would greatly benefit from an efficient gene delivery system that can enhance transfection and effectiveness. As an alternative to growth factor-mediated bone regeneration, viral and nonviral gene delivery methods have been used to deliver vectors carrying plasmids that encode osteogenic molecules, such as *miR-200c* [32]. Viral vectors have a high transfection efficiency but are costly and difficult to produce, and they are further limited by issues with carcinogenesis and immunogenesis [33]. Recently, nonviral vectors, such as high-molecular weight, branched polyethylenimine (PEI), have become increasingly popular for pDNA delivery, as they circumvent the safety concerns and limitations of viral methods [34,35]. PEI transfection efficiencies are high among the nonviral methods; however, PEI has been found to be cytotoxic and shows limited biodegradability [36]. Alternatively, calcium phosphates (CaPs) have been used for decades as effective gene carriers to introduce pDNA into many cell types through CaP/pDNA coprecipitation [37–39]. More recently, $CaCO_3$, a well-studied mineral biomaterial, has demonstrated excellent osteoconductivity, biocompatibility and biodegradability and possesses significant applicability for gene delivery in bone regeneration [40,41]. As a nanoparticle, $CaCO_3$ can easily be coprecipitated with pDNA to form a nanocomplex system for gene delivery. Furthermore, coprecipitation of $CaCO_3$ with protamine sulfate (PS), a clinically used antidote for heparin-induced anticoagulation, has been found to substantially improve $CaCO_3$-mediated pDNA transfer into cells [42–44]; however, its efficacy for gene delivery and tissue regeneration *in vivo* has not been studied. This evidence strongly suggests that $CaCO_3$/PS nanoparticle composites have the potential to deliver pDNA encoding *miR-200c* to promote osteogenic differentiation and bone formation to restore bone defects caused by craniofacial reconstructive surgeries.

In this study, the authors investigated bone formation induced by $CaCO_3$/*miR-200c* coprecipitation under both *in vitro* and *in vivo* conditions. They found that the $CaCO_3$/*miR-200c* nanocomplexes significantly increased *miR-200c* expression in human embryonic palatal mesenchymal (HEPM) cells and sustained the overexpression with no inflammatory or cytotoxic effects. They also found that their $CaCO_3$/*miR-200c* nanocomplexes significantly increased *in vivo* bone formation in their alveolar bone defect model. These findings attest to the regenerative

capacity of *miR-200c* in restoring large bone defects and further indicate its potential application to the treatment of craniofacial bone defects from reconstructive surgeries.

Materials & methods

Preparation & characterization of the CaCO$_3$/pDNA nanocomplex

CaCO$_3$/pDNA nanocomplexes were created by incorporating pDNA into CaCO$_3$/PS coprecipitated nanoparticles via a self-assembly method based on previous literature [38,42–46]. Two separately prepared solutions were combined to form the nanocomplexes. Specifically, pDNA encoding *miR-200c* at different doses was mixed with 16 μl of CaCl$_2$ (0.5 M) and then diluted to a final volume of 60 μl (solution A). Solution B was prepared by mixing 16 μl of NaCO$_3$ (0.01 M) with PS at different doses and then diluting it to a total volume of 40 μl. Solutions A and B were mixed to produce the CaCO$_3$/PS/*miR-200c* nanocomplexes. The CaCO$_3$/pDNA nanocomplexes were visualized using field-emission scanning electron microscopy (FE-SEM; Hitachi S-4800, Tokyo, Japan).

The hydrodynamic particle diameter and zeta potential of the CaCO$_3$/pDNA nanocomplexes were measured using dynamic light scattering (DLS; Zetasizer Nano ZS; Malvern Instruments, Worcestershire, UK). To assess hydrodynamic diameter, a 0.5 mg/ml solution of the CaCO$_3$/pDNA nanocomplexes in a 5 mM HEPES buffer ([4-(2-hydroxyethyl)-1-piperazineethanesulfonic acid]; Thermo Fisher Scientific, MA, USA) at pH 7 was placed in a disposable cuvette for DLS measurements in backscattering mode (173°). Calcite was assumed to be the primary crystal form of the nanoparticles, with an ordinary refractive index of 1.486 and an absorption of 0.1. Water at 20°C was the main component of the dispersant and resulted in a viscosity of 1.0031 cP and refractive index of 1.330. DLS data revealed both primary and aggregated nanoparticle distributions. The primary nanoparticle distribution was analyzed using a modified Gaussian function in Origin 2018. To assess the zeta potential of the nanocomplexes, surface potential was calculated as the average of two measurements at pH 7 and pH 9 at 20°C using the same DLS device and operating parameters, only substituting the cuvette to a DTS1060 cell.

Transfection efficiency of pDNA encoding *miR-200c* influenced by ratios of CaCO$_3$:PS

The authors used preosteoblast, HEPM cells (ATCC, VA, USA), to determine the transfection efficiency of pDNA encoding *miR-200c* using the CaCO$_3$/pDNA nanocomplex delivery system. HEPM cells were cultured and expanded in DMEM supplemented with 10% fetal bovine serum and 1% penicillin-streptomycin (Life Technologies, NY, USA) at 37°C, 5% CO$_2$. To determine the influence of CaCO$_3$:PS ratio on *miR-200c* transfection efficiency, the authors transfected HEPM cells (2×10^4 cells/well; 12-well plate) with CaCO$_3$/PS nanoparticles incorporating pDNA encoding *miR-200c* at different CaCO$_3$:PS ratios (1:0.03125, 1:0.125, 1:0.25 and 1:0.5). For CaCO$_3$/*miR-200c* transfection, HEPM cells were transfected with CaCO$_3$/*miR-200c* nanocomplex (1 μg) in 1 ml Gibco™ Minimal Essential Medium (Opti-MEM®; Thermo Fisher Scientific) for 16 h, after which the transfecting medium was replaced with fresh DMEM Complete Medium for continued cell culture. After 3 days, the transfection efficiency of the CaCO$_3$/*miR-200c* nanocomplexes with differing PS ratios was assessed via quantitative reverse transcription PCR (qRT-PCR; performed using technical triplicates).

Analysis of transfection efficiency of pDNA encoding *miR-200c* delivered by CaCO$_3$-based nanoparticle systems

To determine the transfection efficiency of the authors' CaCO$_3$/*miR-200c* nanocomplexes and to compare them with other delivery systems, the authors transfected HEPM cells (2×10^4 cells/well; 12-well plate) with pDNA encoding empty vector (EV) or *miR-200c* using naked pDNA alone, branched PEI (MW: 25 kDa; Sigma-Aldrich, MO, USA) or CaCO$_3$/PS coprecipitated nanoparticles. For this study, the seven treatment groups included: 1) untreated control; 2, 3) naked pDNA encoding EV or *miR-200c* (1 μg); 4, 5) PEI/pDNA nanocomplex encoding EV or *miR-200c* (1 μg); and 6, 7) CaCO$_3$/pDNA nanocomplex encoding EV or *miR-200c* (1 μg).

For naked pDNA transfection, HEPM cells were transfected with naked pDNA encoding EV or *miR-200c* (1 μg) in 1 ml Opti-MEM® for 16 h, after which the transfecting medium was replaced with fresh DMEM Complete Medium for continued cell culture. For PEI transfection, the PEI/pDNA (3:1 ratio) nanocomplex was formed by adding 4 μg of PEI solution to 1 μg of pDNA encoding *miR-200c* solution, and the combined solution was mixed via pipetting for 30 s. The PEI/pDNA mixture was then incubated at room temperature for 30 min to allow for nanocomplex formation. The HEPM cells were transfected using PEI/pDNA nanocomplex encoding EV or *miR-200c* (1 μg) in 1 ml Opti-MEM® for 6 h, after which the transfecting media was replaced with fresh DMEM Complete Medium for continued cell culture. For the CaCO$_3$/pDNA nanocomplex transfection,

Table 1. Primer sequences used for *in vitro* quantitative reverse transcription PCR analyses.

Gene	Forward primer	Reverse primer
GAPDH	5′-CATCACTGCCACCCAGAAGACTG-3′	5′-ATGCCAGTGAGCTTCCCGTTCAG-3′
IL-6	5′-ACTCACCTCTTCAGAACGAATTG-3′	5′-CCATCTTTGGAAGGTTCAGGTTG-3′
IL-8	5′-ACTGAGGATTGAGAGTGGAC-3′	5′-AACCCTCTGCACCCAGTTTTC-3′

CaCO$_3$/pDNA nanocomplexes were formed as previously described using a 1:0.25 CaCO$_3$:PS ratio, and HEPM cells were transfected with CaCO$_3$/pDNA nanocomplexes encoding EV or *miR-200c* (1 µg) in 1 ml Opti-MEM® for 16 h, after which the transfecting medium was replaced with fresh DMEM Complete Medium for continued cell culture. After 3 days, *miR-200c* transfection efficiency induced by the different delivery systems was assessed via qRT-PCR, using the methods previously described (performed using technical triplicates).

Analysis of biocompatibility of pDNA encoding *miR-200c* delivered by CaCO$_3$-based nanoparticle systems

The influence of the nonviral delivery systems on the viability of transfected HEPM cells was assessed via a MTT cell viability assay kit according to the manufacturer's protocol (Biotium, CA, USA). HEPM cells were seeded into 96-well plates (5 × 10^3 cells/well) and transfected, as previously described, with either pDNA encoding EV or *miR-200c* (0.1 µg) using the nonviral delivery system (either PEI or CaCO$_3$/PS nanoparticles), with untreated HEPM cells as the control group. The transfected cells were then cultured for 3 days, after which MTT solution was added and absorbance was measured and normalized to the untreated control HEPM cells following manufacturer protocol on a spectrophotometer (SpectraMax iD3; Molecular Devices, CA, USA) at 570 nm, with background absorbance set to 630 nm.

The authors also quantified proinflammatory cytokines induced by nonviral delivery systems. HEPM cells transfected with naked pDNA, PEI or CaCO$_3$ nanocomplex were cultured in DMEM Complete Medium for 3 days and the mRNA of inflammatory biomarkers for *IL-6* and *IL-8* was evaluated via qRT-PCR (each treatment performed using technical triplicates).

qRT-PCR analysis for *miR-200c* & inflammatory biomarker expression

Total cellular RNA from cultured HEPM cells was extracted using a miRNeasy Mini Kit (Qiagen, CA, USA). The concentration and purity of total RNA were quantified using a NanoDrop™ One Microvolume UV-Vis Spectrophotometer (Thermo Fisher Scientific). To measure *miR-200c* expression, the mirScript II reverse transcription kit and the mirScript SYBR Green PCR Kit (Qiagen) were used and normalized to *GAPDH*, an internal control for human cells, via a comparative Ct (ΔΔCt) method. Expression of *IL-6* and *IL-8* was performed on a CFX Connect™ (Bio-Rad, CA, USA) using the SYBER® Premix Ex Taq™ II Kit (Takara Bio, Inc, Kusatsu, Japan). Gene expression was calculated and compared with *GAPDH* via a comparative Ct (ΔΔCt) method. The primer sequences are listed in Table 1.

Evaluating the release of CaCO$_3$/*miR-200c* from collagen sponges

To investigate the differences in release of pDNA from collagen sponges with different delivery systems, the authors quantified pDNA release profiles and the cellular uptake of pDNA encoding *miR-200c* released from collagen sponges incorporating naked pDNA or CaCO$_3$/pDNA nanocomplexes across different time points. To study pDNA release, collagen sponges were incorporated with either naked pDNA encoding *miR-200c* (10 µg) or CaCO$_3$/pDNA nanocomplexes encoding *miR-200c* (10 µg). Similarly, to evaluate cellular uptake of released pDNA encoding *miR-200c*, collagen sponges were incorporated with either naked pDNA (5 µg), or CaCO$_3$/pDNA nanocomplexes encoding *miR-200c* (5 µg; n = 3/condition). For both studies, collagen sponges were loaded with either treatment (20 µl/sponge), then lyophilized overnight. Each sponge was then placed into a 1.5 ml tube filled with 500 µl phosphate-buffered saline (PBS) and placed on a shaker to continuously shake at 150 r.p.m. and 4°C for the duration of each study. For the release study, at each time point, half of the PBS solution was removed for dsDNA analysis and fresh PBS solution was added back to the tube. The concentration of pDNA released from the sponges was quantified using a Qubit™ dsDNA HS Assay Kit (Invitrogen, MA, USA) at distinct time points following the manufacturer's protocols. For the cellular uptake study, at each time point, the collagen sponges were removed from the PBS solution and subsequently seeded with HEPM cells (5 × 10^5 cells/sponge).

The cellular uptake of pDNA encoding *miR-200c* by the HEPM cells in relation to the release of naked pDNA or CaCO$_3$/pDNA nanocomplexes from the collagen sponges was measured using qRT-PCR after 48 h.

Tooth socket model: surgical preparation & animal care

All *in vivo* animal experiments were performed under the approval from the Office of Animal Resources at the University of Iowa. The surgical protocols were followed by the policies and guidelines provided by the Institutional Animal Care and Use Committee and all animal surgeries were performed under sterile conditions. All biological agents (pDNAs, CaCO$_3$ etc.) and collagen sponges were prepared and implanted into 12-week-old male Sprague Dawley rats (Charles River Laboratories, MA, USA) under sterile conditions in a surgical environment. Under general anesthesia using ketamine/xylazine, the maxillary teeth and surrounding tissues were disinfected with 2% iodine tincture. After the first molar (M1) was removed on the left and right sides of the maxilla, a 2-mm-wide by 1 mm-deep hole was created in the alveolar bone of the molar cavity using a 2 mm implant twist drill. The cavity was then filled with an experimental treatment group (n = 3–5/treatment): no treatment (defect control); collagen sponge incorporating CaCO$_3$/pDNA nanocomplexes encoding EV (0.1 μg); or collagen sponge incorporating CaCO$_3$/pDNA nanocomplexes encoding *miR-200c* (0.1 μg). Each animal received one treatment per maxillary side. After treatment designation and implantation, each cavity was sutured closed. The rats were euthanized after 3 weeks, and full maxillary palates containing the M1 alveolar bone implants were harvested. Harvested tissues were first rinsed in PBS, then fixed in 4% paraformaldehyde.

## *miR-200c* tooth socket micro-computed tomography imaging & quantification

Micro-computed tomography (μCT) imaging was performed to evaluate new bone formation within the tooth socket defect space. Images of the tooth socket defects were scanned and reconstructed via a μCT scanner with Bruker software (Skyscan model 1272; Bruker, Kontich, Belgium) using the following acquisition parameters: 70 kV, 142 μA, 0.6 rotation step, 1 mm Al filter and 14 μm pixel size. Dragonfly 2021.3 software (Object Research Systems, Montreal, Canada) was then used to analyze bone formation in the socket defects. Briefly, reconstructed palatal images were loaded into Dragonfly and, using grayscale intensity thresholding, low-density soft tissues were removed and a dataset including all dense bone materials was created. After thresholding, a spherical, 0.75-mm-diameter region of interest (ROI) was placed in the defect space to emulate the defect created by the dental burr. The spherical ROI was cut in half across the native alveolar bone line running across the top of the defect, thus creating a 1-mm-wide by 0.75-mm-deep defect ROI, which was used to evaluate bone growth in the defect region. Bone formation in the defects was collected as a volume percentage of dense bone dataset values within the defect ROI. Bone volume data were collected in this manner, utilizing the same thresholds, across all samples, and representative 2D and 3D images were acquired to visualize bone formation in the defects.

Histological evaluation of *in vivo* bone formation in tooth socket defects

The explanted maxillas were decalcified for 8 h using a decalcification solution (Decalcifying Solution–Lite; Sigma-Aldrich). The decalcified samples were then cleared with xylene and embedded in paraffin. The entire embedded sample, which included the defect with collagen sponge implant and surrounding maxillary tissue, was cut into 7 μm coronal sections and stained with hematoxylin and eosin and Masson's trichrome stain using standard protocols. Representative sections were selected for staining at distinct intervals throughout the sample, starting from the middle of the sample and working outward at an interval sampling distance of 0.1 mm (n = 5). Corresponding images of the stained tissues were taken using an inverted microscope (Eclipse Ts2; Nikon Instruments, Inc, NY, USA) to examine the bone formation occurring from the treated collagen sponge within the tooth socket defect.

Statistical analysis

Descriptive statistics were conducted for both *in vitro* and *in vivo* investigations. A one-way analysis of variance with *post hoc* Tukey's honestly significant difference test was used to determine whether there was a significant difference between treatment groups for both the *in vitro miR-200c* transfection and biocompatibility studies. For the *in vivo* study, a one-way analysis of variance with *post hoc* Tukey's honestly significant difference test was utilized to evaluate whether there were significant differences in bone formation across treatment groups. The Shapiro–Wilks test was also applied to verify the assumption of normality. All statistical tests completed for the *in vitro* and *in vivo* quantifications used a significance level of 0.05, and each graphic depicts mean values and associated standard
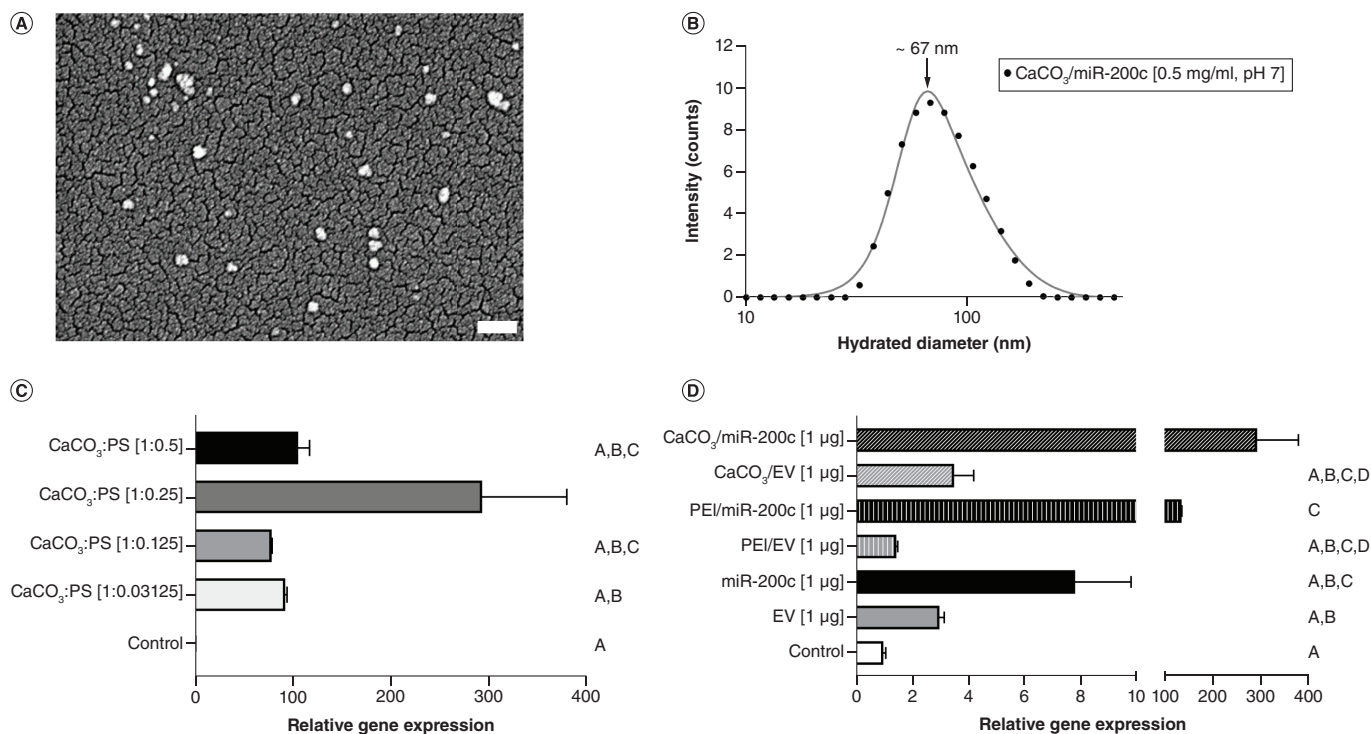
Figure 1.   Characterization of CaCO₃/*miR-200c* nanocomplex particles and evaluation of *miR-200c* transfection efficiency using CaCO₃ nanoparticles in comparison with naked plasmid DNA and polyethylenimine transfection. (A) Scanning electron microscopy image of CaCO₃/*miR-200c* nanocomplex particles. **(B)** Analysis of the hydrodynamic particle diameter for the CaCO₃/*miR-200c* nanocomplex particles measured via dynamic light scattering. **(C)** Relative expression levels of *miR-200c* from human embryonic palatal mesenchymal cells cultured for 3 days after transfection with different CaCO₃:protamine sulfate ratios. **(D)** Relative expression levels of *miR-200c* from human embryonic palatal mesenchymal cells cultured for 3 days after transfection using different transfection systems. Column means that do not share a letter are statistically significantly different using the *post hoc* Tukey's honestly significant difference test ($p < 0.05$; performed in triplicate). Scale bar: 100 nm.
EV: Empty vector; PEI: Polyethylenimine; PS: Protamine sulfate.

deviations. Statistical analyses and associated figures were created via GraphPad Prism (version 8.1.2.; GraphPad Software, Inc., CA, USA).

Results

CaCO₃ as a nonviral delivery system efficiently delivers pDNA encoding *miR-200c*

CaCO₃/*miR-200c* nanocomplexes were created by incorporating pDNA encoding *miR-200c* into CaCO₃/PS coprecipitated nanoparticles via a self-assembly method. The CaCO₃/*miR-200c* nanocomplexes were observed via SEM imaging to have a well-defined, reproducible, rhombohedral geometry characteristic of the calcite crystalline phase of CaCO₃, with the nanocomplexes displaying an average diameter of 32 nm (Figure 1A). Hydrated CaCO₃/*miR-200c* nanocomplexes exhibited a hydrodynamic diameter of 67 nm with a zeta potential of -5.17 mV (Figure 1B). After characterizing the CaCO₃/*miR-200c* nanocomplexes, the authors evaluated how the CaCO₃:PS ratio influenced *miR-200c* transfection of HEPM cells *in vitro*. They found that the CaCO₃:PS ratio of 1:0.25 statistically significantly increased expression of *miR-200c* in comparison with untreated control HEPM cells (**$p < 0.01$) as well as all other tested CaCO₃:PS ratios (*$p < 0.05$; Figure 1C). No significant differences were observed between the control HEPM cells and all other tested CaCO₃:PS ratios. From these results, the authors investigated the transfection efficiency of the CaCO₃/*miR-200c* nanocomplexes with the optimized CaCO₃:PS ratio (1:0.25) in comparison with other transfection methods using nonviral delivery systems such as naked pDNA and PEI. The authors found that transfecting HEPM cells with CaCO₃/*miR-200c* statistically significantly increased *miR-200c* expression in comparison with untreated control HEPM cells and all other nonviral transfection systems, including naked pDNA and PEI (***$p < 0.001$; Figure 1D). Furthermore, PEI/*miR-200c* transfection statistically significantly increased *miR-200c* expression in HEPM cells compared with untreated control HEPM
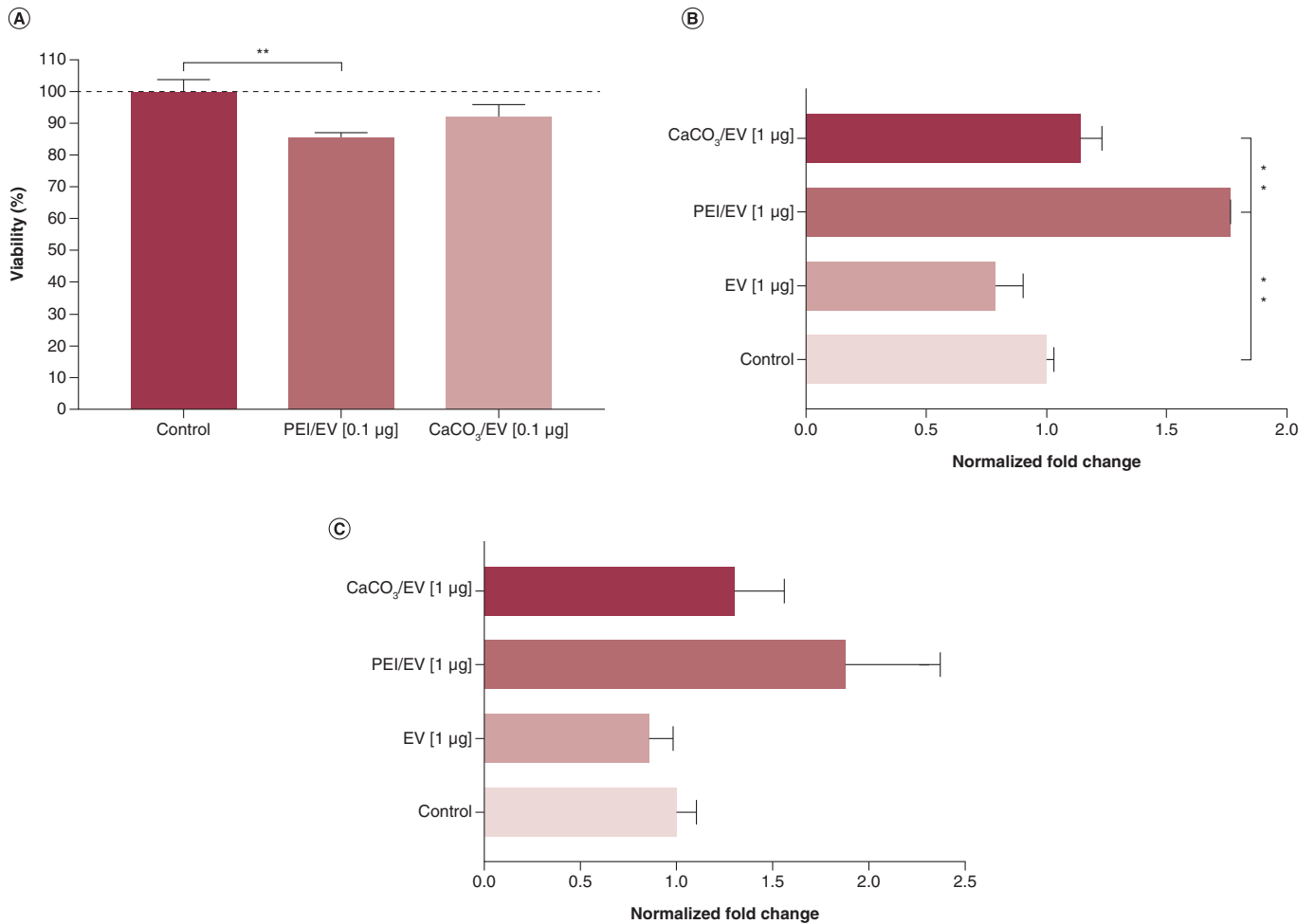
Figure 2.   **Assessment of inflammatory and cytotoxic effects of nonviral CaCO$_3$ and polyethylenimine nanoparticle delivery systems. (A)** Evaluation of the biocompatibility of different nonviral delivery systems with human embryonic palatal mesenchymal cells assessed via MTT assay (**p $<$ 0.01; performed in triplicate). **(B & C)** Normalized fold change of *IL-6* **(B)** and *IL-8* **(C)** transcripts from human embryonic palatal mesenchymal cells 3 days after transfection with different delivery systems.
**p $<$ 0.01; performed in triplicate.
EV: Empty vector; PEI: Polyethylenimine.

cells and naked pDNA transfection (*p $<$ 0.05); however, *miR-200c* expression by PEI/*miR-200c* transfection was statistically significantly less than that of CaCO$_3$/*miR-200c* transfection (*p $<$ 0.05). Transfection with naked pDNA encoding *miR-200c* increased *miR-200c* expression in comparison with untreated control HEPM cells and HEPM cells transfected with naked pDNA encoding EV, PEI/EV and CaCO$_3$/EV; however, this increase in *miR-200c* expression was not significant. There were additionally no observable differences in *miR-200c* expression found when comparing untreated HEPM control cells and delivery systems using pDNA encoding EV.

The CaCO$_3$-based nanoparticle delivery system is highly biocompatible

Biocompatibility of the different nonviral delivery systems was assessed via an MTT assay and proinflammatory marker quantification via qRT-PCR using HEPM cells. Cytotoxicity of the PEI and CaCO$_3$ nanocomplex delivery systems was evaluated by an MTT assay 3 days after initial HEPM cell transfection with each delivery system (Figure 2A). Untreated HEPM cells were used as a control. After 3 days, the viability of HEPM cells treated with the CaCO$_3$/EV nanocomplex was not significantly reduced in comparison with untreated HEPM control cells. However, HEPM cells transfected with the PEI/EV system exhibited a statistically significant reduction in cell viability after 3 days compared with untreated HEPM cells (**p $<$ 0.01).

Proinflammatory marker expression for *IL-6* (Figure 2B) and *IL-8* (Figure 2C) was quantified via qRT-PCR 3 days after HEPM cell transfection with naked pDNA encoding EV, PEI/EV or $CaCO_3$/EV nanocomplex, with untreated HEPM cells as the control. After 3 days of culture, the HEPM cells transfected with the PEI/EV system exhibited a statistically significant increase in *IL-6* expression in comparison with untreated HEPM cells and $CaCO_3$/EV nanocomplex transfected cells (**$p < 0.01$) and HEPM cells transfected with naked pDNA encoding EV (***$p < 0.001$). HEPM cells transfected with the $CaCO_3$/EV nanocomplex did not significantly increase *IL-6* expression in comparison with untreated HEPM control cells. Furthermore, after 3 days of culture, the HEPM cells transfected with the PEI/EV system showed an increase in *IL-8* expression in comparison with untreated HEPM control cells and HEPM cells transfected with either naked pDNA encoding EV or $CaCO_3$/EV nanocomplex; however, this increase in *IL-8* expression was not significant. HEPM cells transfected with the $CaCO_3$/EV nanocomplex additionally did not significantly increase *IL-8* expression in comparison with untreated HEPM control cells.

$CaCO_3$-based nanoparticles extend the overexpression of *miR-200c* in collagen sponges *in vitro*
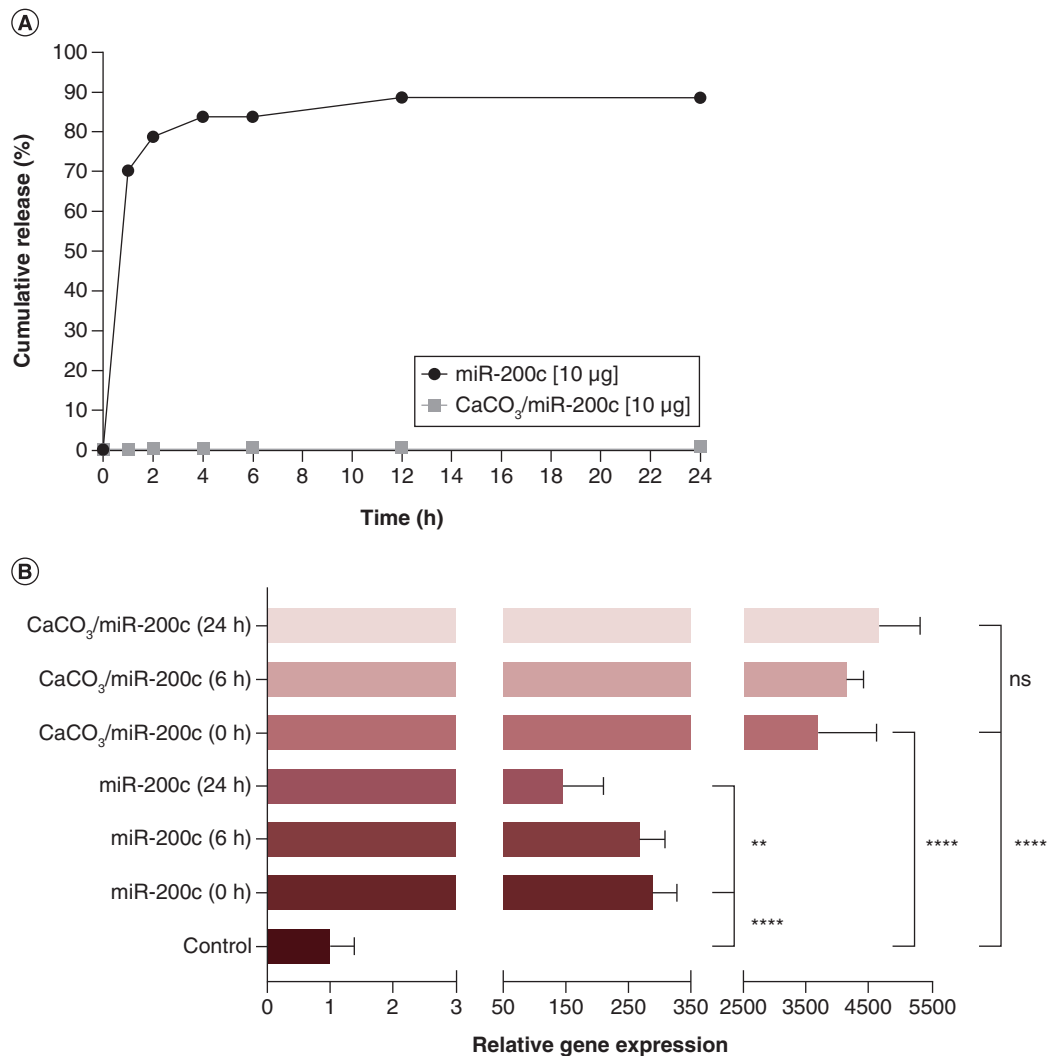
pDNA release from collagen sponges incorporating naked pDNA encoding *miR-200c* or $CaCO_3$/*miR-200c* nanocomplex was quantified using a high-sensitivity dsDNA kit (Figure 3A). From the authors' release study, they found that naked pDNA was rapidly released from the collagen sponges, with an approximately 83.78% cumulative release of naked pDNA after 6 h and 88.59% cumulative release after 24 h. However, limited release of *miR-200c* from the collagen sponges incorporating $CaCO_3$/*miR-200c* nanocomplexes was measured after 24 h. For the cellular uptake study, HEPM cells were seeded onto collagen sponges incorporating either naked pDNA encoding *miR-200c* or $CaCO_3$/*miR-200c* nanocomplexes that had been placed in PBS solution to release incorporated components for 0, 6 or 24 h (Figure 3B). The authors found that HEPM cells seeded on the $CaCO_3$/*miR-200c* nanocomplex-incorporated collagen sponges significantly increased *miR-200c* overexpression about ten-times higher than collagen sponges incorporating naked pDNA encoding *miR-200c* (****$p < 0.0001$) and approximately 4500-times higher than collagen sponge control samples (****$p < 0.0001$). Furthermore, the extent of *miR-200c* overexpression in HEPM cells was not decreased significantly during the extended time period when the $CaCO_3$/*miR-200c* nanocomplex-incorporated collagen sponges were immersed in PBS solution. The collagen sponges incorporating naked pDNA encoding *miR-200c* also significantly increased *miR-200c* overexpression in the seeded HEPM cells compared with the HEPM cell-seeded collagen control sponges (****$p < 0.0001$); however, the collagen sponges incorporating naked pDNA encoding *miR-200c* displayed a significant decrease in *miR-200c* overexpression in HEPM cells after 24 h in PBS solution compared with 0-h and 6-h time points (**$p < 0.01$).

$CaCO_3$/pDNA *miR-200c* nanocomplexes enhance alveolar bone formation *in vivo*

The capacity of the $CaCO_3$/pDNA nanocomplex system to promote *in vivo* bone formation was evaluated using an M1 tooth socket defect rat model. Collagen sponges incorporated with $CaCO_3$/EV (1 μg) or $CaCO_3$/*miR-200c* (1 μg) were implanted into M1 tooth socket defects in rats for 3 weeks, after which alveolar bone formation was assessed via μCT imaging (Figure 4A) and bone volume percentage quantification (Figure 4B). Through μCT imaging, the authors were able to visualize bone tissue growth within the defect space of the M1 tooth socket. They found that the untreated defect samples visually presented the least amount of bone formation in comparison with the samples treated with collagen sponges incorporating either $CaCO_3$/EV or $CaCO_3$/*miR-200c*. Furthermore, based on μCT imaging alone, the defects treated with $CaCO_3$/*miR-200c* displayed the greatest amount of bone formation within the regenerating defect space in comparison with the untreated and $CaCO_3$/EV treated defects. This visually observable increase in bone formation for the $CaCO_3$/*miR-200c* treated defects was quantitatively confirmed using μCT quantitative analysis, in which new bone formation occurring in the defect space was measured as a bone volume percentage. Based on the quantitative analysis, the authors found that defects treated with collagen sponges incorporating $CaCO_3$/*miR-200c* had a statistically significantly increased production of new bone formation (50.88%) in comparison with untreated defects (22.29%; *$p < 0.05$) and defects treated with collagen sponges incorporating $CaCO_3$/EV (16.53%; **$p < 0.01$). No significant differences were found in bone volume percentage between the untreated defects and the defects treated with collagen sponges incorporating $CaCO_3$/EV.

After μCT imaging and quantitative analysis, the explanted palates were sectioned and stained for histological examination. In the hematoxylin and eosin- and Masson's trichrome-stained sections (Figure 5), the authors

Figure 3.   Quantification of naked *miR-200c* and CaCO$_3$/*miR-200c* nanocomplex release from collagen sponges and their effect on *miR-200c* overexpression. (A) Release profile of naked plasmid DNA encoding *miR-200c* and CaCO$_3$/*miR-200c* nanocomplexes from collagen sponges over 24 h. **(B)** *miR-200c* overexpression in human embryonic palatal mesenchymal cells seeded on collagen sponges incorporating naked plasmid DNA encoding *miR-200c* or CaCO$_3$/*miR-200c* nanocomplexes across different release time points.
**p $<$ 0.01; ****p $<$ 0.0001; n = 2/treatment, performed in duplicate.
ns: Not significant.

observed limited areas of scattered bone formation in the untreated defects and the defects treated with collagen sponges incorporating CaCO$_3$/EV. Instead, for these two groups, they observed more fibrous tissue formation than new bone formation. However, in the defects treated with collagen sponges incorporating CaCO$_3$/*miR-200c*, they observed increased amounts of new bone formation within the defect space with minimal fibrous tissue formation.

Discussion

The development of advanced exogenous therapeutics with strong osteogenic properties that enhance bone formation is necessary to effectively treat craniofacial bone defects caused by diseases that require reconstructive surgery. This study, for the first time, revealed that CaCO$_3$/*miR-200c* nanocomplexes formed through the coprecipitation of osteogenic *miR-200c* with CaCO$_3$ nanoparticles significantly improve cell transfection, increase cellular *miR-200c* overexpression and enhance bone formation in a rat alveolar bone tooth socket defect model. These findings demonstrate the safe, potent and restorative capabilities of *miR-200c* when used with CaCO$_3$ nanoparticles to en-
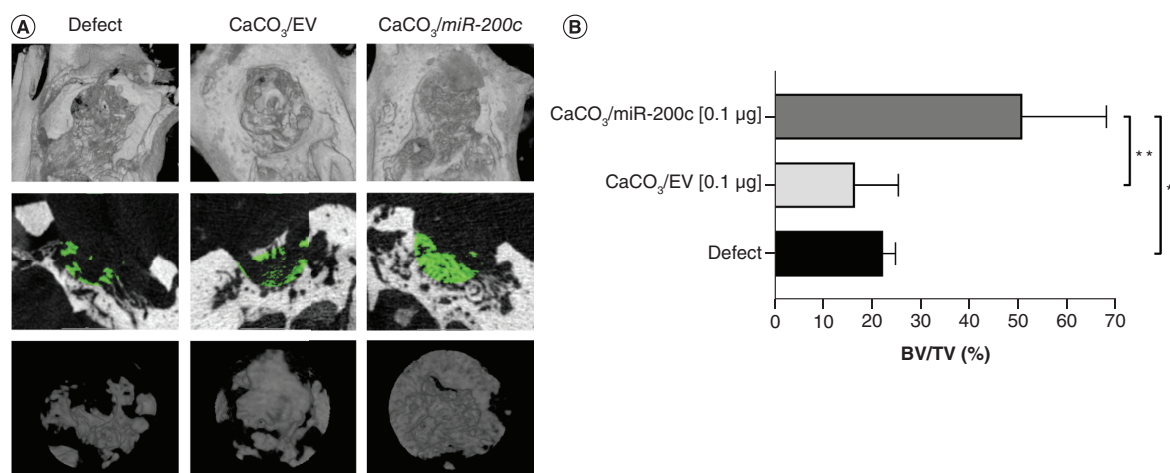
Figure 4.   Micro-computed tomography analysis of bone formation induced by collagen sponges incorporating CaCO₃/*miR-200c* nanocomplexes in maxillary tooth socket bone defects. (A) Representative micro-computed tomography images of the top and cross-sectional views displaying new bone formation (green) observed in maxillary tooth socket defects with different treatments 3 weeks post-treatment. **(B)** Quantitative analysis of bone volume percentage in defects with different treatments.
*$p < 0.05$; **$p < 0.01$; n = 3–5.
BV: Bone volume; EV: Empty vector; TV: Tissue volume.
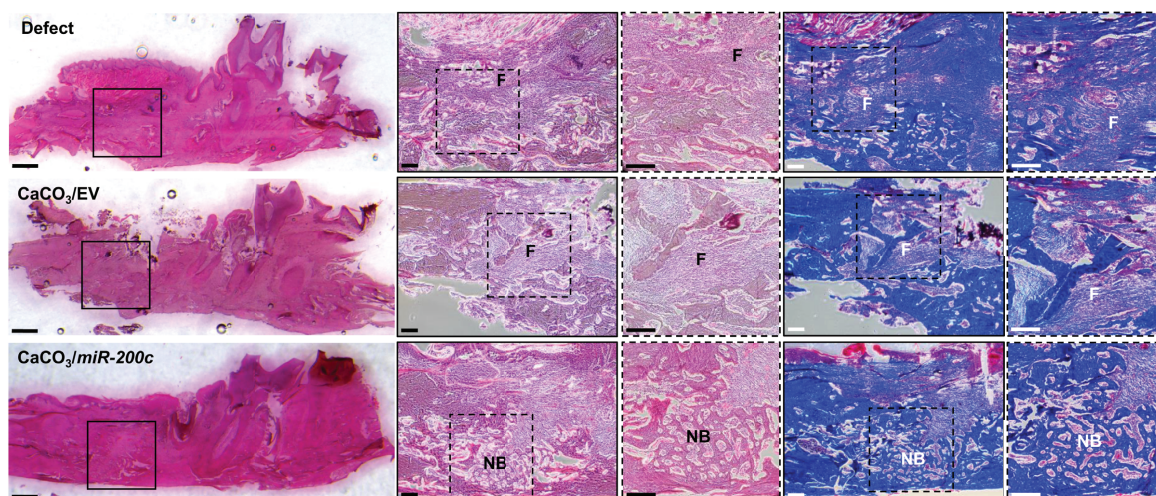
Figure 5.   Histological analysis of new bone formation induced by collagen sponges incorporating CaCO₃/*miR-200c* nanocomplexes in maxillary tooth socket bone defects. Microphotographs of the cross sections of tooth socket defects with different treatments stained by hematoxylin and eosin and Masson's trichrome staining at different magnifications. Scale bars: 1 mm (1×), 200 μm (4×, 10×).
EV: Empty vector; F: Fibrous tissues; NB: New bone.

hance bone formation in large defects. These results significantly advance the potential of miR-based therapeutics for clinical bone formation.

In overcoming the challenges of growth factor-based regenerative strategies, miRs have emerged as critical osteogenic biomolecules to enhance bone formation. In this study, the authors coprecipitated CaCO₃ with pDNA encoding *miR-200c* to create CaCO₃/*miR-200c* nanocomplexes. To characterize the morphology and particle diameter of both dried and hydrated CaCO₃/*miR-200c* nanocomplexes, the authors utilized SEM imaging and DLS. Using SEM, they found that their CaCO₃/*miR-200c* nanocomplexes had an average diameter of 32 nm, which is well within the reported 1–100 nm nanoparticle diameter range (Figure 1A). Furthermore, they observed the CaCO₃/*miR-200c* nanocomplexes to have a characteristic nanoscale size and rhombohedral morphology

consistent with the calcite crystalline phase of CaCO$_3$ using SEM imaging. Several prior studies have determined that the combination of CaCl$_2$ and Na$_2$CO$_3$ precursors in the presence of water without cell culture medium or polyphosphate creates the calcite crystalline phase of CaCO$_3$ [47–51]. Calcite is thermodynamically stable and is reported to not dissolve in cell culture medium, which the authors observed in this study. Combined with these published findings, the present study's CaCO$_3$ preparation protocol and SEM images indicate that the CaCO$_3$ nanocomplexes formed in this study are characteristic of the calcite crystalline phase of CaCO$_3$; however, further analyses using x-ray diffraction and Fourier transform infrared spectroscopy should be performed to confirm the crystalline phase. Using DLS, the authors determined that the CaCO$_3$/*miR-200c* nanocomplexes had a surface charge zeta potential of -5.17 mV (Figure 1B). It is reported that particles with zeta potentials beyond ±30 mV are typically considered stable; however, for particles with zeta potentials between ±30 mV, electrostatic repulsive forces alone are insufficient to promote long-term stability of particles, leading to an increased likelihood for particle aggregation with time [52–54]. The low zeta potential of the present study's CaCO$_3$ nanocomplexes could cause particles to aggregate over time and at higher particle concentrations, and DLS is reported to have limited accuracy in measuring aggregated samples with high polydispersity indexes [55–57]. Therefore, the authors of the present study used freshly prepared, low-concentration (0.5 mg/ml) CaCO$_3$ samples in HEPES buffer for the DLS measurements and found that the CaCO$_3$ nanocomplexes had a hydrodynamic particle diameter size of 67 nm (Figure 1B). They further found that with increased measurement time (i.e., greater than 30 min) and CaCO$_3$ concentration, the measured polydispersity index increased, indicating the aggregation of CaCO$_3$ particles. The authors also observed that the solvent composition influenced the tendency of the particles to aggregate; HEPES-buffered CaCO$_3$ nanocomplexes displayed a low polydispersity index with limited aggregation in comparison with CaCO$_3$ particles measured in PBS solution that displayed high polydispersity and rapid, uncontrolled aggregation. Evidence from prior studies indicates that pH, the concentration of H$^+$ ions and the presence or absence of proteins in the suspending medium greatly influence particle surface potential, stability and ultimately quantification capabilities via DLS [58]. One study found that the presence of bovine serum albumin in cell culture medium increased colloidal stability and hindered particle aggregation [59]. The present study's results further indicate that solvent choice influences particle aggregation and ultimately affects DLS measurement capabilities.

Previous studies utilizing CaCO$_3$ for gene delivery have coprecipitated CaCO$_3$ with PS to significantly improve CaCO$_3$-mediated pDNA transfer into cells. The present study found that the optimal CaCO$_3$:PS ratio to significantly enhance *miR-200c* transfection into HEPM cells was 1:0.25 (Figure 1C). Utilizing this optimal ratio, the authors successfully found that the CaCO$_3$/*miR-200c* nanocomplexes significantly increased *miR-200c* transfection into HEPM cells in comparison with PEI and naked pDNA transfection (Figure 1D). PEI transfection also increased *miR-200c* expression in HEPM cells but to a significantly lesser degree than that of the CaCO$_3$/*miR-200c* nanocomplexes. These results demonstrate that through using an optimized CaCO$_3$:PS ratio, CaCO$_3$/*miR-200c* nanocomplexes can be effectively developed to significantly enhance *miR-200c* transfection. Based on the authors' previous work with *miR-200c*, they have found that transfection via naked pDNA encoding *miR-200c* significantly increases *miR-200c* in both human and rat BMSCs and increases the expression of osteogenic markers, including *RUNX2*, *OCN* and *OPG*. The authors chose to use HEPM cells for this study because they have previously confirmed *miR-200c* expression outcomes in human and rat BMSCs and wanted to test human preosteoblasts. Based on their previously published findings, they believe the significantly amplified *miR-200c* expression in HEPM cells transfected via their CaCO$_3$/*miR-200c* nanocomplexes would also increase osteogenic marker expression in HEPM cells in a similar manner to their prior results using BMSCs.

This study evaluated the biocompatibility of CaCO$_3$/*miR-200c* nanocomplexes in relation to other nonviral transfection methods. The authors again utilized HEPM cells, as the results from this human-derived cell line would be translatable to clinical situations with human patients. From the MTT assay, the authors determined that CaCO$_3$ nanocomplex transfection did not affect HEPM cell viability in comparison with untreated cells (Figure 2A). HEPM cells transfected via CaCO$_3$/*miR-200c* nanocomplexes also did not significantly increase the expression of *IL-6* or *IL-8* in comparison with untreated cells (Figure 2B & C). PEI transfection, however, significantly increased *IL-6* expression in comparison with untreated cells and CaCO$_3$/*miR-200c*-transfected cells. PEI transfection also increased *IL-8* expression, but not significantly. These data indicate that these CaCO$_3$/*miR-200c* nanocomplexes are biocompatible, noncytotoxic and safe for human cell transfection. The results also affirm evidence published in the literature and further substantiate the cytotoxic and proinflammatory properties of PEI as a nonviral transfection mechanism.

Based on the authors' previous study demonstrating the slow-release potential of collagen coatings, they evaluated the influence of collagen on the release of their nanocomplexes [21]. The CaCO$_3$/*miR-200c* nanocomplexes were developed from published protocols, yet few studies have evaluated the release profile of CaCO$_3$/pDNA nanoparticles. For the authors' release study, they utilized a high-sensitivity dsDNA assay kit to measure pDNA release, which uses fluorescent probes to tag dsDNA for quantification. The authors found that naked pDNA encoding *miR-200c* incorporated into collagen sponges was rapidly released over 24 h but observed limited release of CaCO$_3$/*miR-200c* (Figure 3A). The small amount of pDNA released from the CaCO$_3$/*miR-200c*-incorporated collagen samples could be explained by an inability of the fluorescent probe of the dsDNA kit to effectively tag pDNA bound to CaCO$_3$ nanoparticles. Coprecipitation of pDNA with CaCO$_3$ nanoparticles creates a CaCO$_3$/pDNA polymer network in which the pDNA polymer is surrounded by CaCO$_3$ nanoparticles and the electrostatic interactions between the CaCO$_3$ and pDNA polymer chain create a condensed polymer network [60]. The binding of CaCO$_3$ nanoparticles to the pDNA polymer chain may have limited the ability of the fluorescent probe to effectively tag pDNA bound to CaCO$_3$ nanoparticles released from the collagen sponges. This may explain why few studies have published results for pDNA release from CaCO$_3$ nanoparticles, as current methods require the dissociation of pDNA from CaCO$_3$ for effective quantification. One previous study evaluated pDNA release from CaP-based nanoparticles by using two different pH-buffered solutions to dissolve nanoparticles prior to dsDNA quantification [41]. However, the authors of the present study could not effectively use this method to measure released dsDNA, possibly due to differences between the previous studies' CaP and the present study's CaCO$_3$ nanoparticles. In order to test whether there is an interaction between the collagen and CaCO$_3$/*miR-200c* nanocomplexes that extends the release of the nanocomplexes, the authors seeded HEPM cells onto naked pDNA and CaCO$_3$/*miR-200c*-incorporated collagen sponges that had been immersed into PBS for 0, 6 or 24 h. Using this approach, they quantified the cellular uptake of pDNA remaining in collagen after PBS exposure at different time points as an indicator of naked pDNA or CaCO$_3$/*miR-200c* release from the collagen sponges (Figure 3B). They further found a significant decrease in *miR-200c* expression for the naked *miR-200c*-collagen sponges after 24 h in PBS, indicating that pDNA was released from these samples and this depletion decreased the ability of the HEPM cells to amplify *miR-200c* overexpression to the same extent as the 0-h and 6-h samples. However, there were no significant differences in *miR-200c* overexpression for CaCO$_3$/*miR-200c*-collagen after 0, 6 and 24 h in PBS, suggesting that the release of nanocomplexes from collagen is sustained for 24 h. The dissimilarities in the release of naked pDNA and CaCO$_3$/pDNA from collagen sponges are likely due to differences in electrostatic interactions and pDNA encapsulation by the CaCO$_3$ nanoparticles. The quick release of pDNA from the collagen sponge is likely due to electrostatic repulsive forces between the negatively charged pDNA molecules and the negatively charged collagen protein. For the CaCO$_3$/pDNA samples, however, coprecipitation of pDNA with CaCO$_3$ nanoparticles created a nanocomplex system that encapsulated pDNA within the CaCO$_3$ nanoparticles and likely slowed and sustained pDNA release over time as the CaCO$_3$ particles dissolved [61,62].

The authors' prior published studies used naked pDNA encoding *miR-200c* delivered via bulbus injections, *miR-200c*-incorporated collagen sponges and, more recently, 3D-printed *miR-200c*-incorporated collagen-coated scaffolds to regenerate large and critical-sized bone defects. From these studies, they have demonstrated the osteogenic and anti-inflammatory properties of *miR-200c* and have found that *miR-200c* can effectively induce bone formation in rat calvarial defect models using these different *miR-200c* delivery approaches. However, like the authors' prior works, most published studies only utilize calvarial models to study bone formation. To regenerate defects caused by diseases such as oral cancer, there is a need to use *in vivo* models that more appropriately mimic the conditions of craniofacial reconstructive surgery, such as in an alveolar bone defect model. Few published studies have used tooth socket defect models to study alveolar bone regeneration and, to the authors' knowledge, none have used miRs to enhance alveolar bone formation, until now. The present study utilized an M1 tooth socket defect model to investigate the capacity of CaCO$_3$/*miR-200c* nanocomplexes to enhance alveolar bone formation. Based on the μCT imaging and quantification results (Figure 4), they found that the CaCO$_3$/*miR-200c*-incorporated collagen sponges significantly increased the percentage of new bone formation in the alveolar bone defects in comparison with untreated defects and defects treated with collagen sponges incorporating CaCO$_3$/EV. They further confirmed this increase in new bone formation in the CaCO$_3$/*miR-200c*-treated samples via hematoxylin and eosin and Masson's trichrome staining (Figure 5). In the histology sections, they observed more new bone formation in the alveolar bone defects treated with CaCO$_3$/*miR-200c*-incorporated collagen sponges, whereas the untreated defects and defects treated with CaCO$_3$/EV-incorporated collagen sponges displayed more fibrous tissue assembly than new bone formation. In prior studies, the authors assessed bone formation at longer time

intervals, such as after 6 weeks. However, in this study, they were interested in determining if the $CaCO_3$/*miR-200c* nanocomplexes could induce bone regeneration at earlier stages and, thus, decided to assess regeneration after 3 weeks. The authors assume that with longer implantation times, they would find increased bone formation across all samples, with the defects treated with $CaCO_3$/*miR-200c*-incorporated collage sponges displaying significantly more bone formation; however, additional, longer-term studies would need to be completed to confirm this. The data from this study indicate that the $CaCO_3$/*miR-200c* nanocomplexes significantly enhance alveolar bone formation *in vivo*. These results further attest to the osteogenic and regenerative properties of *miR-200c* and build upon the conclusions of the authors' previous *in vivo* studies using *miR-200c* for calvarial bone regeneration. In congruence with the previous findings, data from this study support *miR-200c* as a potent and effective osteogenic agent that has significant application in treating different types of craniofacial bone defects.

    The findings of this study demonstrate that $CaCO_3$/*miR-200c* nanocomplexes significantly enhance the transfection of *miR-200c* into HEPM cells in a biocompatible and noncytotoxic manner. These data establish the $CaCO_3$/pDNA nanocomplex system as an effective tool for nonviral gene delivery and a safer alternative to PEI transfection. Furthermore, $CaCO_3$ nanoparticles can effectively sustain the release of *miR-200c* from collagen sponges and extend enhanced expression of *miR-200c in vitro*. The results of the *in vivo* study also demonstrate that the $CaCO_3$/*miR-200c* nanocomplexes can effectively enhance bone formation in an alveolar bone defect model, further authenticating *miR-200c* as a potent osteogenic agent applicable to craniofacial bone restoration. This evidence strongly indicates that $CaCO_3$/*miR-200c* nanocomplexes significantly enhance transfection of pDNA encoding *miR-200c* into cells to promote osteogenesis and bone formation and effectively illustrates the therapeutic potential of *miR-200c* to restore bone defects caused by craniofacial reconstructive surgeries and diseases.

Conclusion

There is a critical need to develop advanced osteogenic therapeutics to effectively regenerate bone defects caused by craniofacial diseases such as oral cancer. miRNAs, specifically *miR-200c*, are biomolecules with potent osteogenic and anticancer properties that have significant application as novel regenerative agents to treat craniofacial bone defects. In this study, we successfully demonstrated that $CaCO_3$/*miR-200c* nanocomplexes significantly enhance plasmid transfection in a noncytotoxic, biocompatible manner in comparison with naked pDNA- and PEI-based transfection strategies. We further demonstrated, for the first time, that $CaCO_3$/*miR-200c* nanocomplexes significantly enhance *in vivo* bone formation in an alveolar bone defect model. These results strongly support $CaCO_3$-based nanoparticles as a safe and efficient nonviral system for cellular plasmid delivery and further advance the clinical potential of miR-based regenerative strategies to restore craniofacial bone defects.

Summary points

- Craniofacial bone defects are surgically and therapeutically challenging to treat, and current regenerative methods are limited in their abilities to safely and effectively restore large bone defects.
- miRNAs play crucial roles in craniofacial bone development and regeneration, and *miR-200c* has been found to effectively enhance osteogenesis and *in vivo* bone regeneration to heal bone defects.
- $CaCO_3$-based nanoparticles have recently been utilized as nonviral vectors for plasmid DNA-based cell transfection; however, their efficiency *in vivo* and biocompatibility in comparison with other nonviral strategies have yet to be determined.
- Coprecipitation of $CaCO_3$ with protamine sulfate at an optimal ratio increases human embryonic palatal mesenchymal cell transfection.
- $CaCO_3$/*miR-200c* nanocomplexes created via the coprecipitation of $CaCO_3$/protamine sulfate with plasmid DNA encoding *miR-200c* enhances *miR-200c* transfection into human embryonic palatal mesenchymal cells.
- $CaCO_3$ nanocomplexes are biocompatible and noncytotoxic, unlike polyethylenimine transfection.
- $CaCO_3$/*miR-200c* nanocomplexes enhance *in vivo* bone formation in an alveolar bone defect model.
- These results support *miR-200c* as a safe, potent and restorative osteogenic agent that when used in combination with $CaCO_3$ nanoparticles enhances *in vivo* bone formation in large craniofacial defects.
- These findings attest to the robust osteogenic properties of *miR-200c* for enhancing bone regeneration and further illustrate the potential clinical application of miR-based therapeutics in treating large craniofacial bone defects.

Ethical conduct of research

The authors state that they have obtained appropriate institutional review board approval or have followed the principles outlined in the Declaration of Helsinki for all human or animal experimental investigations.

References

Papers of special note have been highlighted as: ● of interest; ●● of considerable interest

1. Chen Y-L, Kuo S-W, Fang K-H, Hao S-P. Prognostic impact of marginal mandibulectomy in the presence of superficial bone invasion and the nononcologic outcome. *Head Neck* 33(5), 708–713 (2011).

2. Ebrahimi A, Murali R, Gao K, Elliott MS, Clark JR. The prognostic and staging implications of bone invasion in oral squamous cell carcinoma. *Cancer* 117(19), 4460–4467 (2011).

3. Elmusrati AA, Pilborough AE, Khurram SA, Lambert DW. Cancer-associated fibroblasts promote bone invasion in oral squamous cell carcinoma. *Br. J. Cancer* 117(6), 867–875 (2017).

4. Grammatica A, Piazza C, Pellini R *et al.* Free flaps for advanced oral cancer in the "older old" and "oldest old": a retrospective multi-institutional study. *Front. Oncol.* 9, 604 (2019).

5. Knitschke M, Sonnabend S, Bäcker C *et al.* Partial and total flap failure after fibula free flap in head and neck reconstructive surgery: retrospective analysis of 180 flaps over 19 years. *Cancers* 13(4), 865 (2021).

6. Kumar BP, Venkatesh V, Kumar KAJ, Yadav BY, Mohan SR. Mandibular reconstruction: overview. *J. Maxillofac. Oral Surg.* 15(4), 425–441 (2016).

7. Koller M, Rafter D, Shok G, Murphy S, Kiaei S, Samadani U. A retrospective descriptive study of cranioplasty failure rates and contributing factors in novel 3D printed calcium phosphate implants compared to traditional materials. *3D Print. Med.* 6(1), 14 (2020).

8. Garland CB, Pomerantz JH. Regenerative strategies for craniofacial disorders. *Front. Physiol.* 3, 14 (2012).

9. Chinn SB, Myers JN. Oral cavity carcinoma: current management, controversies, and future directions. *J. Clin. Oncol.* 33(29), 3269–3276 (2015).

● Describes the key aspects of diagnosing, treating and managing oral cancers; provides data on recurrence rates and treatment efficiencies; and describes impactful studies advancing the field.

10. Chung Y-I, Ahn K-M, Jeon S-H, Lee S-Y, Lee J-H, Tae G. Enhanced bone regeneration with BMP-2 loaded functional nanoparticle-hydrogel complex. *J. Control. Release* 121(1), 91–99 (2007).

11. Li L, Zhou G, Wang Y, Yang G, Ding S, Zhou S. Controlled dual delivery of BMP-2 and dexamethasone by nanoparticle-embedded electrospun nanofibers for the efficient repair of critical-sized rat calvarial defect. *Biomaterials* 37, 218–229 (2015).

12. Mitchell AC, Briquez PS, Hubbell JA, Cochran JR. Engineering growth factors for regenerative medicine applications. *Acta Biomater.* 30, 1–12 (2016).

13. Vijayavenkataraman S, Yan W-C, Lu WF, Wang C-H, Fuh JYH. 3D bioprinting of tissues and organs for regenerative medicine. *Adv. Drug Delivery Rev.* 132, 296–332 (2018).

14. Aguilar LMC, Silva SM, Moulton SE. Growth factor delivery: defining the next generation platforms for tissue engineering. *J. Control. Release* 306, 40–58 (2019).

15. D'cruz AK, Vaish R, Dhar H. Oral cancers: current status. *Oral Oncol.* 87, 64–69 (2018).

16. Peng SP, Gao D, Gao CD, Wei PP, Niu M, Shuai CJ. MicroRNAs regulate signaling pathways in osteogenic differentiation of mesenchymal stem cells (review). *Mol. Med. Rep.* 14(1), 623–629 (2016).

17. Lian JB, Stein GS, Van Wijnen AJ *et al.* MicroRNA control of bone formation and homeostasis. *Nat. Rev. Endocrinol.* 8(4), 212–227 (2012).

18. Arriaga MA, Ding M-H, Gutierrez AS, Chew SA. The application of microRNAs in biomaterial scaffold-based therapies for bone tissue engineering. *Biotechnol. J.* 14(10), 1900084 (2019).

19. Catalanotto C, Cogoni C, Zardo G. MicroRNA in control of gene expression: an overview of nuclear functions. *Int. J. Mol. Sci.* 17(10), 1712 (2016).

20. Hong L, Sun H, Amendt BA. MicroRNA function in craniofacial bone formation, regeneration and repair. *Bone* 144, 115789 (2021).
●● **Illustrates the mechanisms of miRNAs in regulating bone formation and describes advances in miRNA-based technologies for bone regeneration.**

21. Remy MT, Akkouch A, He L *et al.* Rat calvarial bone regeneration by 3D-printed β-tricalcium phosphate incorporating *microRNA-200c*. *ACS Biomater. Sci. Eng.* 7(9), 4521–4534 (2021).
●● **Study investigates *miR-200c* as an osteoinductive agent for bone regeneration using 3D-printed bone grafts and evaluates transfection efficiency, release profile and osteogenic capacity of *miR-200c* under both *in vitro* and *in vivo* conditions.**

22. Akkouch A, Eliason S, Sweat ME *et al.* Enhancement of *microRNA-200c* on osteogenic differentiation and bone regeneration by targeting SOX2-mediated WNT signaling and KLF4. *Hum. Gene Ther.* 30(11), 1405–1418 (2019).
●● **Provides experimental evidence that evaluates the molecular mechanisms regulating *miR-200c*-based bone regeneration and illustrates the influence of miRNAs on craniofacial bone development in mice.**

23. Cao H, Jheon A, Li X *et al.* The pitx2:Mir-200c/141:Noggin pathway regulates BMP signaling and ameloblast differentiation. *Development* 140(16), 3348–3359 (2013).

24. Hill L, Browne G, Tulchinsky E. Zeb/mir-200 feedback loop: at the crossroads of signal transduction in cancer. *Int. J. Cancer* 132(4), 745–754 (2013).

25. Humphries B, Yang C. The microRNA-200 family: small molecules with novel roles in cancer development, progression and therapy. *Oncotarget* 6(9), 6472–6498 (2015).

26. Katoh Y, Katoh M. Hedgehog signaling, epithelial-to-mesenchymal transition and miRNA (review). *Int. J. Mol. Med.* 22(3), 271–275 (2008).

27. Vallejo DM, Caparros E, Dominguez M. Targeting notch signalling by the conserved mir-8/200 microRNA family in development and cancer cells. *EMBO J.* 30(4), 756–769 (2011).

28. Krongbaramee T, Zhu M, Qian Q *et al.* Plasmid encoding *microRNA-200c* ameliorates periodontitis and systemic inflammation in obese mice. *Mol. Ther. Nucleic Acids* 23, 1204–1216 (2021).

29. Akkouch A, Zhu M, Romero-Bustillos M *et al.* MicroRNA-200c attenuates periodontitis by modulating proinflammatory and osteoclastogenic mediators. *Stem Cells Dev.* 28(15), 1026–1036 (2019).
●● **Study provides experimental data indicating the mechanistic involvement of *miR-200c* in modulating cytokine production and inflammation associated with periodontal disease.**

30. Hong L, Sharp T, Khorsand B *et al.* MicroRNA-200c represses IL-6, IL-8, and CCL-5 expression and enhances osteogenic differentiation. *PLOS ONE* 11(8), e0160915 (2016).

31. Chuang TD, Khorram O. *miR-200c* regulates IL8 expression by targeting ikbkb: a potential mediator of inflammation in leiomyoma pathogenesis. *PLOS ONE* 9(4), (2014).

32. Kimelman Bleich N, Kallai I, Lieberman JR, Schwarz EM, Pelled G, Gazit D. Gene therapy approaches to regenerating bone. *Adv. Drug Delivery Rev.* 64(12), 1320–1330 (2012).

33. Pack DW, Hoffman AS, Pun S, Stayton PS. Design and development of polymers for gene delivery. *Nat. Rev. Drug Discov.* 4(7), 581–593 (2005).

34. Acri TM, Laird NZ, Jaidev LR, Meyerholz DK, Salem AK, Shin K. Nonviral gene delivery embedded in biomimetically mineralized matrices for bone tissue engineering. *Tissue Eng. Part A* 27(15-16), 1074–1083 (2020).

35. Yin H, Kanasty RL, Eltoukhy AA, Vegas AJ, Dorkin JR, Anderson DG. Non-viral vectors for gene-based therapy. *Nat. Rev. Genet.* 15(8), 541–555 (2014).

36. Son S, Namgung R, Kim J, Singha K, Kim WJ. Bioreducible polymers for gene silencing and delivery. *Acc. Chem. Res.* 45(7), 1100–1112 (2012).

37.   Liu Y, Yu B, Dai X, Zhao N, Xu F-J. Biomineralized calcium carbonate nanohybrids for mild photothermal heating-enhanced gene therapy. *Biomaterials* 274, 120885 (2021).

38.   Zhao D, Wang C-Q, Zhuo R-X, Cheng S-X. Modification of nanostructured calcium carbonate for efficient gene delivery. *Colloids Surf. B.* 118, 111–116 (2014).

39.   Jhill M, Qi B, Bayaniahangar R *et al.* Nanomaterials for bone tissue regeneration: updates and future perspectives. *Nanomedicine (Lond.)* 14(22), 2987–3006 (2019).

40.   Chen C, Han HF, Yang W, Ren XY, Kong XD. Polyethyleneimine-modified calcium carbonate nanoparticles for p53 gene delivery. *Regen. Biomater.* 3(1), 57–63 (2016).

41.   Zhao M, Li J, Chen D, Hu H. A valid bisphosphonate modified calcium phosphate-based gene delivery system: increased stability and enhanced transfection efficiency *in vitro* and *in vivo*. *Pharmaceutics* 11(9), 468 (2019).

42.   Wang CQ, Gong MQ, Wu JL, Zhuo RX, Cheng SX. Dual-functionalized calcium carbonate based gene delivery system for efficient gene delivery. *RCS Adv.* 4(73), 38623–38629 (2014).

43.   He X-Y, Liu B-Y, Xu C, Zhuo R-X, Cheng S-X. A multi-functional macrophage and tumor targeting gene delivery system for the regulation of macrophage polarity and reversal of cancer immunoresistance. *Nanoscale* 10(33), 15578–15587 (2018).

44.   Wang CQ, Wu JL, Zhuo RX, Cheng SX. Protamine sulfate-calcium carbonate-plasmid DNA ternary nanoparticles for efficient gene delivery. *Mol. BioSyst.* 10(3), 672–678 (2014).

••   **Describes the methods used to create the CaCO₃/protamine sulfate/plasmid DNA nanocomplexes used in this work.**

45.   Zhao D, Zhuo RX, Cheng SX. Alginate modified nanostructured calcium carbonate with enhanced delivery efficiency for gene and drug delivery. *Mol. BioSyst.* 8(3), 753–759 (2012).

46.   Zhao D, Liu CJ, Zhuo RX, Cheng SX. Alginate/CaCO₃ hybrid nanoparticles for efficient codelivery of antitumor gene and drug. *Mol. Pharm.* 9(10), 2887–2893 (2012).

47.   Zou Z, Bertinetti L, Politi Y *et al.* Opposite particle size effect on amorphous calcium carbonate crystallization in water and during heating in air. *Chem. Mater.* 27(12), 4237–4246 (2015).

48.   Borah BM, Dey SK, Das G. Crystal to calcite: fabrication of pure calcium carbonate polymorph in the solid state. *Cryst. Growth Des.* 11(7), 2773–2779 (2011).

49.   Konrad F, Gallien F, Gerard DE, Dietzel M. Transformation of amorphous calcium carbonate in air. *Cryst. Growth Des.* 16(11), 6310–6317 (2016).

50.   Tolba E, Müller WEG, Abd El-Hady BM *et al.* High biocompatibility and improved osteogenic potential of amorphous calcium carbonate/vaterite. *J. Mater. Chem. B* 4(3), 376–386 (2016).

51.   Ihli J, Wong WC, Noel EH *et al.* Dehydration and crystallization of amorphous calcium carbonate in solution and in air. *Nat. Commun.* 5(1), 3169 (2014).

52.   Clogston JD, Patri AK. Zeta potential measurement. In: *Characterization of Nanoparticles Intended for Drug Delivery.* McNneil SE (Ed.). Humana Press, NJ, USA, 63–70 (2011).

53.   Haddad Z, Abid C, Oztop HF, Mataoui A. A review on how the researchers prepare their nanofluids. *Int. J. Therm. Sci.* 76, 168–189 (2014).

54.   Rasmussen MK, Pedersen JN, Marie R. Size and surface charge characterization of nanoparticles with a salt gradient. *Nat. Commun.* 11(1), 2337 (2020).

55.   Bhattacharjee S. DLS and zeta potential – what they are and what they are not. *J. Control. Release* 235, 337–351 (2016).

56.   Shang L, Nienhaus K, Nienhaus GU. Engineered nanoparticles interacting with cells: size matters. *J. Nanobiotechnol.* 12(1), 5 (2014).

57.   Hoo CM, Starostin N, West P, Mecartney ML. A comparison of atomic force microscopy (AFM) and dynamic light scattering (DLS) methods to characterize nanoparticle size distributions. *J. Nanopart. Res.* 10(1), 89–96 (2008).

58.   Cho EJ, Holback H, Liu KC, Abouelmagd SA, Park J, Yeo Y. Nanoparticle characterization: state of the art, challenges, and emerging technologies. *Mol. Pharm.* 10(6), 2093–2110 (2013).

59.   Lauth V, Maas M, Rezwan K. An evaluation of colloidal and crystalline properties of CaCO₃ nanoparticles for biological applications. *Mat. Sci. Eng. C.* 78, 305–314 (2017).

•   **Provides key insights into designing drug delivery systems using CaCO₃-based nanoparticles and evaluates the material properties and characterization of CaCO₃ crystalline morphologies.**

60.   Xu Y, Tijssen KCH, Bomans PHH *et al.* Microscopic structure of the polymer-induced liquid precursor for calcium carbonate. *Nat. Commun.* 9(1), 2582 (2018).

•   **Describes the interactions of CaCO₃ particles with dsDNA in forming nanocomplex polymer network systems.**

61.   Tovani CB, Zancanela DC, Fafria AN, Ciancaglini P, Ramos AP. Bio-inspired synthesis of hybrid tube-like structures based on CaCO₃ and type I-collagen. *RCS Adv.* 6(93), 90509–90515 (2016).

62.   Katana B, Rouster P, Varga G *et al.* Self-assembly of protamine biomacromolecule on halloysite nanotubes for immobilization of superoxide dismutase enzyme. *ACS Appl. Bio Mater.* 3(1), 522–530 (2020).